Geophysical Journal International

Geophys. J. Int. (2020) **222,** 1–14
Advance Access publication 2020 March 14
GJI Seismology

doi: 10.1093/gji/ggaa113

An array-based receiver function deconvolution method: methodology and application

Minyan Zhong and Zhongwen Zhan

Seismological Laboratory, California Institute of Technology, Pasadena, CA 91125*, USA. E-mail: minyan.zhong@gmail.com*

Accepted 2020 March 7. Received 2020 March 7; in original form 2019 June 24

SUMMARY

Receiver functions (RFs) estimated on dense arrays have been widely used for the study of Earth structures across multiple scales. However, due to the ill-posedness of deconvolution, RF estimation faces challenges such as non-uniqueness and data overfitting. In this paper, we present an array-based RF deconvolution method in the context of emerging dense arrays. We propose to exploit the wavefield coherency along a dense array by joint inversions of waveforms from multiple events and stations for RFs with a minimum number of phases required by data. The new method can effectively reduce the instability of deconvolution and help retrieve RFs with higher fidelity. We test the algorithm on synthetic waveforms and show that it produces RFs with higher interpretability than those by the conventional RF estimation practice. Then we apply the method to real data from the 2016 Incorporated Research Institutions for Seismology (IRIS) community wavefield experiment in Oklahoma and are able to generate high-resolution RF profiles with only three teleseismic earthquakes recorded by the temporary deployment. This new method should help enhance RF images derived from short-term high-density seismic profiles.

Key words: Joint inversion; Time-series analysis; Computational seismology.

1 INTRODUCTION

Receiver function (RF) has been an indispensable tool in global seismology. The classical teleseismic *P*-wave RF isolates receiver-side structures from source and path effects by deconvolving vertical component (*Z*) from radial component (*R*) (e.g. Vinnik 1977; Langston 1979; Ammon 1991). RF has been applied routinely to study crustal and upper mantle structures, such as basins, Moho and subduction zones (e.g. Zhu & Kanamori 2000; Nábelek *et al.* 2009; Nikulin *et al.* 2009; Levander *et al.* 2011; Ma & Clayton 2016). The classical RF has also been generalized to longer periods and *S* waves, to study the lithosphere–asthenosphere–boundary (LAB) and the mantle transition zones (e.g. Fischer *et al.* 2010; Miller & Piana Agostinetti 2012; Tauzin *et al.* 2013). In particular, wide applications of RF on dense arrays have pushed Earth structure images to unprecedented resolutions (e.g. IRIS Portable Array Seismic Studies of the Continental Lithosphere (PASSCAL) experiments in United States, Tibet and South America, and the EarthScope Transportable and Flexible arrays; Eagar *et al.* 2011; Kumar *et al.* 2012; Levander & Miller 2012; Shen *et al.* 2013; Tauzin *et al.* 2013; Schulte-Pelkum & Mahan 2014).

In this paper, we focus on RF estimation along a dense profile of stations, a common layout of seismic experiments to get a cross-section of target areas (e.g. Nábelek *et al.* 2009; Kim *et al.* 2010; Ma & Clayton 2016). The conventional practice is that RFs are estimated independently at individual stations and are then combined to form a 2-D RF profile. The coherent phases on the profile are then tracked and interpreted as structural discontinuities. To improve the RF resolution, it is common to stack individual RFs obtained from many events that share similar receiver-side structural responses. In RF imaging, the next step is to relate RFs to physical structures through migrating or inverting RFs for reflectivity and velocity models. (e.g. Ammon *et al.* 1990; Dueker & Sheehan 1997; Zhu & Kanamori 2000; Gilbert *et al.* 2003; Xu *et al.* 2013). The new method we present here is solely on RF estimation using arrays, not on deriving reflectivity or velocity models from the RFs.

Although dense-array RFs are widely used to reveal Earth discontinuities, it is well known that obtaining high-resolution RF profiles is far from being trivial and sometimes challenging. This reason is often related to the ill-posedness of deconvolution, or more specifically non-uniqueness and data overfitting. As a result, RFs often include spurious phases and are difficult to interpret. These issues related to RF deconvolution have been widely recognized and there have been many efforts in overcoming the challenges, which we summarize as the following three categories:

1. Procedures for data and RF quality controls, especially for (semi-) automated systems. For example, the IRIS EARS project has a conservative system rating the RFs (Crotwell & Owens 2005). Yang *et al.* (2016) developed a RF quality control system with 13 procedures. The chosen criteria need to account for the time-span of

seismic experiments as well as the quantity and quality of available data.

2. Improved algorithms to stabilize the RF deconvolution. The most classical one is water-level spectral division (Clayton & Wiggins 1976). The multitaper approach provides optimal spectra estimates by suppressing stochastic effects thus further improving spectral division (Park & Levin 2000). Time-domain iterative deconvolution is probably the most widely used RF method these days, due to its simplicity, robustness at suppressing ringing effects and ability to obtain consistent RFs from events of different source spectra (Ligorría & Ammon 1999). Gurrola *et al.* (1995) performed the time-domain deconvolution as a regularized simultaneous inversion of a group of events, to improve stability and suppress artifacts. Recently, more sophisticated statistical deconvolution methods are proposed, involving Bayesian inference and time series sparsity modelling (Yildirim *et al.* 2010, Kolb & Lekić 2014).

3. Stacking and post-processing of RFs. Stacking has been the most common approach to improve RF quality. RFs estimated from a group of events sharing receiver-side structural response are combined, often through some kind of averaging, to produce the stacked one with random noise suppressed. When it comes to RFs on dense arrays, RF post-processing can be another way towards the same goal. For example, Wilson & Aster (2005) applied frequency–wavenumber (FK) filter to 2-D RF profiles to promote spatial coherency. On a dense nodal seismic array, Ward *et al.* (2018) averaged individual RFs within 10 km to suppress noise and produce coherent RF images.

In this paper, we propose a new RF deconvolution method towards improving RF estimation on dense arrays. Its main characteristic is to exploit the coherency of dense-array RFs. Fig. 1 is a schematic example of an RF dense array experiment. The incoming teleseismic P wave converts to S wave at structural discontinuities. Because of the small station spacing, RFs at nearby stations correspond to similar ray paths and are coherent. The coherency exists for laterally smooth discontinuities, as well as sharp features such as offsets/steps in discontinuities or scatters due to wave diffraction. Therefore, as long as the station spacing is substantially smaller than the depth of structures, the coherency of nearby RFs is maintained.

We will demonstrate that the adoption of coherency can effectively address instabilities in deconvolution. Intuitively, this is because the noise (e.g. instrumental/ambient noise, scattering from shallow/local heterogeneities) are incoherent, while the waveforms constraining RF phases are coherent. Requiring RF to be spatially coherent on a dense array naturally excludes the incoherent parts of waveforms from estimation. Problems, such as non-uniqueness and overfitting, which are essentially related to noise, are thus largely suppressed. Although the idea of combining the power of dense array to RFs is not new, most previous array-based RF methods are actually on how to better translate RFs to subsurface structures (e.g. Dueker & Sheehan 1997; Bostock & Rondenay 1999; Chen *et al.* 2005a, b, Kim *et al.* 2012). For these methods, RFs as the input are assumed to be generated from some standardized procedures. In exploration seismology, multichannel deconvolution has been established (e.g. Wapenaar *et al.* 2011). However, in global seismology, deconvolution on dense-arrays has not systematically moved into an array-based fashion. The aforementioned FK filtering approach (Wilson & Aster 2005) is an early work touching this possibility but focused on post-processing of RFs. The method we propose treats RF coherency more rigorously by integrating it into RF deconvolution.

To include RF coherency into estimation, we cast RF deconvolution as an inverse problem, in which the deconvolution at a single station involves the nearby stations to provide constraints. We design the inverse problem to be sparsity-promoting by parametrizing RFs as a finite number of coherent phases and seek the optimal solution with the minimum number of phases required by data. We also jointly invert seismic data from multiple events, instead of stacking individual RFs, for better stability and rigorous treatment of data uncertainty (Gurrola *et al.* 1995). We adopt the Bayesian formulation of inverse problem which provides the model posterior probability distribution. The optimal RF and RF uncertainties are indicated by the maximum *a posteriori* (MAP) estimation and marginal distributions of parameters.

The structure of the paper is as follows. We first present the methodology in Section 2, including the inverse problem setup and the algorithm for parameter estimation. In Section 3, we show a synthetic test, where we compare this new method with conventional RF practices. Section 4 is a real data application to the 2016 IRIS community wavefield experiment in Oklahoma, where we show the challenges the data set poses to convention RF practices and how they are overcome by the new method.

2 METHODOLOGY

2.1 Inverse problem setup: single-station deconvolution

We first describe the inverse problem formulation of single-station deconvolution. It lays down the foundation for the extension to the array-based version in Section 2.2. We start from the simplest form of P-wave RF. Given a pair of vertical and radial component of seismic records at a single station, the problem of P-wave RF deconvolution can be expressed in frequency domain as:

$$R(\omega) = Z(\omega)\, E(\omega) + N(\omega), \tag{1}$$

where R, Z and E are the spectra of the radial component, the vertical component, and the RF, respectively, and N is the spectrum of noise in the radial component. We parametrize the RF by a finite number of delta functions with different amplitudes and timings. Similar parametrization has been widely used in RF methods and proves useful in producing consistent RFs from events of various source spectra (e.g. Ligorría & Ammon 1999; Kolb & Lekić 2014; Wang & Pavlis 2016). With this parametrization, $E(\omega)$ can be written as:

$$E(\omega;\ a_i, t_i) = \sum_{i=1}^{m} a_i \exp(-i\omega t_i), \tag{2}$$

where m is the number of phases, and t_i and a_i are the timing and amplitude of the ith spike. For simplicity, we ignore the normalization factor in the Fourier transform, which is eventually cancelled out in deconvolution. Using eq. (2), we can rewrite eq. (1) as:

$$R(\omega) = Z(\omega) \sum_{i\ =\ 1}^{m} a_i \exp(-i\omega t_i) + N(\omega). \tag{3}$$

We can then solve for the RF parameters t_i, a_i $(i = 1, \ldots, m)$ by minimizing the squared misfit of data and model prediction if m is

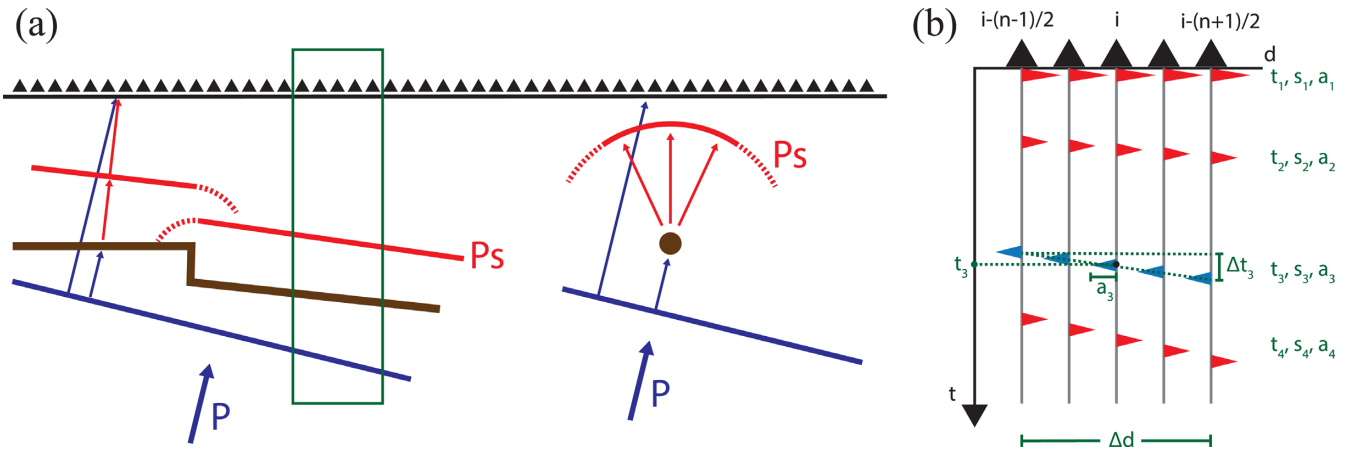

Figure 1. (a) Teleseismic *P* wave (blue) impinges on subsurface structures below a dense seismic profile, including a step along a velocity discontinuity (brown thick lines to the left) and a single scatterer (the brown dot to the right), and generates Ps conversions (red). Due to wave diffraction, the Ps phase recorded by the dense array should be coherent at neighbouring stations. (b) Illustration of coherent RFs for the five-station subarray outlined by the green box in (a). Each coherent RF phase is parametrized by timing t, slowness s and amplitude a. For example, t_3, s_3 and a_3 characterize the negative coherent phase where $s_3 = \Delta t_3/\Delta d$.

known:

$$argmin \left\| R(\omega) - Z(\omega) \sum_{i=1}^{m} a_i \exp(-i\omega t_i) \right\|_2^2 . \quad (4)$$

We can find the optimal m through approaches such as L-curve (Hansen 1992) or cross-validation (Aster *et al.* 2019).

2.2 Inverse problem setup: array-based deconvolution

Array-based deconvolution is built upon the single-station formulation with the consideration of RF coherency. Here, we assume that any specific RF phase has constant amplitude and slowness across a subarray (Fig. 1b). With this assumption, deconvolution at a particular station involves a subarray of stations to provide constraints. For each phase, besides timing and amplitude, now we have an additional parameter, slowness (s). For a subarray with n stations, the spectrum of RF at the jth station ($j = 1, \ldots, n$) is:

$$\mathrm{E_j}(\omega) = \sum_{i=1}^{m} a_i exp\left(-i\omega\left(t_i + s_i\left(x_j - x_c\right)\right)\right), \quad (5)$$

where x_j and x_c are the coordinates of station j and the centre station. Therefore, the array version of eq. (3) for the jth station is

$$\mathrm{R_j}(\omega) = Z_j(\omega) \sum_{i=1}^{m} a_i exp\left(-i\omega\left(t_i + s_i\left(x_j - x_c\right)\right)\right) + N_j(\omega) \quad (j = 1, 2, ..., n). \quad (6)$$

Putting all the n stations within the subarray together, we can write eq. (6) into matrix form

$$\boldsymbol{R} = \boldsymbol{Z}\boldsymbol{E}(\boldsymbol{\theta}) + \boldsymbol{N}. \quad (7)$$

Here, $\boldsymbol{R} = [\boldsymbol{R}_1^T, \boldsymbol{R}_2^T, \ldots, \boldsymbol{R}_n^T]^T$ is a column vector formed by concatenation of the spectra of the radial components at the n stations, where $\boldsymbol{R_j}$ $(1 \le j \le n)$ is a column vector of the spectrum of the radial component at the jth station. $\boldsymbol{Z} = \boldsymbol{diag}([\boldsymbol{Z}_1^T, \boldsymbol{Z}_2^T, \ldots, \boldsymbol{Z}_n^T])$ is a diagonal matrix filled by the spectra of the vertical components at the n stations where $\boldsymbol{Z}_j (1 \le j \le n)$ is a column vector of the spectrum of the vertical component at the jth station. $\boldsymbol{E} = [\boldsymbol{E}_1^T, \boldsymbol{E}_2^T, \ldots, \boldsymbol{E}_n^T]^T$ is a column vector formed by concatenation of the spectra of the n RFs. The RF spectra are parametrized by $\boldsymbol{\theta}$: t_i, s_i and a_i $(i = 1, 2, \ldots, m)$ through (5).

We adopt the Bayesian formulation of inverse problem (Tarantola 2005). Assuming zero-mean Gaussian uncertainties and uniform priors for all parameters, we have the model posterior probability distribution

$$P(\boldsymbol{\theta}|\boldsymbol{R}) \propto P(\boldsymbol{R}|\boldsymbol{\theta}) = \boldsymbol{exp}\left(-\frac{1}{2}(\boldsymbol{R} - \boldsymbol{Z}\boldsymbol{E}(\boldsymbol{\theta}))^T \boldsymbol{C_d}^{-1} (\boldsymbol{R} - \boldsymbol{Z}\boldsymbol{E}(\boldsymbol{\theta}))\right), \quad (8)$$

where $\boldsymbol{C_d}$ is the data covariance matrix. We use a diagonal $\boldsymbol{C_d}$ without consideration of covariance between different frequency. The diagonal entries of $\boldsymbol{C_d}$ are the measurement error variances estimated from the pre-event noise and control how data are weighted. Data is transformed into the frequency domain and all frequencies within the chosen frequency band are jointly inverted for the final RFs. The choice of frequency band depends on the scale of structures, noise level, instrument response, etc., in the same way as in conventional RF estimations. The pursuit of more sophisticated $\boldsymbol{C_d}$ and the incorporation of modelling error (i.e. noise in the vertical components) are potentially important and left for future work (Yagi & Fukahata 2008; Duputel *et al.* 2012). We can find the maximum a posterior (MAP) model estimation through

$$\underset{\boldsymbol{\theta}}{argmin} (\boldsymbol{R} - \boldsymbol{Z}\boldsymbol{E}(\boldsymbol{\theta}))^T \boldsymbol{C_d}^{-1} (\boldsymbol{R} - \boldsymbol{Z}\boldsymbol{E}(\boldsymbol{\theta})). \quad (9)$$

The formulation (7) and (8) above can be extended to jointly invert data from events with similar receiver-side structural responses (Gurrola *et al.* 1995). We prefer joint inversion to stacking the individual inversions for two reasons. First, we can ingest our prior knowledge of the data quality into the estimation rigorously through appropriate design of $\boldsymbol{C_d}$. Secondly, joint inversion helps promote model sparsity by taking all events into consideration simultaneously to constrain the RF phases.

Finally, the choice of subarray size, n, needs to account for two factors. First, the subarray aperture needs to be substantially smaller than the depths of target structures to satisfy our assumption of phase coherency, which states that the phases within a subarray have the same slowness. Secondly, there needs to be enough stations in the subarray to suppress non-uniqueness and overfitting. Therefore, a seismic profile with average station spacing substantially smaller than the depth of target structures would be ideal for applying this array-based deconvolution method. For the synthetic and real-data experiment shown in this paper, we find a five-station subarray setup is optimal. At the two edges of an array, we skip stations that do not have enough nearby stations on both sides to form a subarray.

2.3 Solving the inverse problem: parameter estimation

We employ a derivative-free search method—neighbourhood algorithm (NA)—to find the optimal model by solving (9). NA is a non-linear optimization algorithm developed in Sambridge (1999a). It conducts direct search in the multidimensional parameter space in an iterative fashion. Given a set of initial models, in each iteration, N_s new models are generated from the neighbourhood of the best N_r existing models from the previous iteration. Since NA searches in the full parameter space, the computation complexity increases exponentially with the number of parameters. For computational efficiency, we take advantage of the linearity of the amplitude terms in (5) and rewrite $\boldsymbol{E}(\boldsymbol{\theta})$ in (7) to separate the amplitudes from the nonlinear parameters of timing and slowness:

$$\boldsymbol{E}(\boldsymbol{\theta}) = \boldsymbol{B}(t_1, \ldots, t_m, s_1, \ \ldots, s_m)\,\boldsymbol{A}, \tag{10}$$

where $\boldsymbol{B}$ is the matrix containing the unit spike spectra $\exp(-i\omega(t_i + s_i(x_j - x_c)))$ constructed from the parameters of timing and slowness given the station coordinates $x_1, \ldots, x_n$, and $\boldsymbol{A} = [a_1, \ldots, a_m]^T$ is a column vector of phase amplitudes. Given any particular set of timing and slowness parameters, we can directly find the optimal $\boldsymbol{A}$ through

$$\boldsymbol{A} = ((\boldsymbol{ZB})^T \boldsymbol{C}_d^{-1} (\boldsymbol{ZB}))^{-1} (\boldsymbol{ZB})^T \boldsymbol{C}_d^{-1} \boldsymbol{R}. \tag{11}$$

This separation of linear and nonlinear parameters reduces the number of parameters for the NA non-linear optimization by one third and therefore increases the overall computation efficiency significantly.

To quantify the uncertainty of the RF parameters, we make use of the NA ensemble of searched models, each of which is a sample of the model posterior probability distribution (PPD) given by eq. (8). We use the ensemble appraisal approach introduced in Sambridge (1999b). It first defines an approximate model PPD by interpolating all the samples via Voronoi cells in model space. Gibbs sampler is then used to perform efficient importance sampling of this approximate PPD, from which we can readily find the marginal distribution of parameters.

2.4 Solving the inverse problem: iterative strategy and number of phases

One key parameter in our inverse problem is the number of phases m. It not only controls the computational complexity, but also reflects how many phases the data suggests. We want to design an objective approach to determine m with the goal of sparsity promotion—finding the RF with the smallest number of phases required by data. Our strategy is to iteratively add new phases into the model, until the misfit reduction from adding a new phase is statistically insignificant. In each iteration, we solve for the three parameters (i.e. amplitude, timing and slowness) of the newly added phase, while still adjusting the parameters for the existing phases around their optimal values from the previous iteration. The adjustment of existing phases, which is not included in conventional iterative RF methods (e.g. Ligorría & Ammon 1999), is important because of the possible trade-offs between the new and the existing ones.

As more phases are added to the subarray RFs, the objective function, i.e. the function to minimize in (9), will stabilize/converge. Beyond certain number of phases, any new phases added are overfitting the data. In the conventional iterative time domain method, the number is often set to be large (e.g. 100) to ensure convergence of RF (Ligorría & Ammon 1999). Instead, we stop adding new phases when the distribution of residuals is statistically indistinguishable from the converged/stabilized residual distribution with a large number of phases. Assuming a zero-mean Gaussian data uncertainty $N\left(0, \sigma^2\right)$, our stopping criterion is equivalent to when the σ_m estimated for the RF with m phases is within certain confidential interval of the σ_c estimated for the converged RF. In practice, we first estimate σ_c by adding phases to inversion until convergence. Then we estimate the standard deviation of σ_c for the number of data points we included in inversion by parametric bootstrapping. Finally, we choose the smallest number of phases that bring the σ_m within one standard deviation of σ_c.

Note that the starting assumption of this strategy is that the residuals in the frequency domain follow zero-mean Gaussian distribution. If the spectral power distribution is strongly frequency-dependent, this assumption may not be appropriate. However, additional data pre-processing steps, such as simultaneous spectral whitening of the radial and vertical component, can help mitigate this issue.

3 SYNTHETIC TEST

3.1 Model and synthetics

The synthetic test model is based on a 2-D flat subduction scenario (Fig. 2a), with reference to the central Mexico subduction zone. The oceanic plate first subducts underneath the continental plate with a dipping angle of 17°, then goes flat at 50 km depth for 100 km, and finally plunges into the mantle at 75°. For the continental plate, we set the Moho to have a smooth topography and add a 100-km-long mid-crust discontinuity. The station distribution is similar to the Meso-America Subduction Project (MASE, Kim *et al.* 2010), with an even spacing of 5 km, substantially smaller than the depths of the target structures. We use a 2-D finite difference method (Li *et al.* 2014) to simulate the wavefield from a cluster of seven teleseismic events with the same azimuth aligned with the profile. The epicentre distances are centred at 40° with 2 km spacing. Fig. 2(b) is a snapshot of the simulated wavefield for one of the events. Each event has its unique source time function and therefore different frequency contents. We apply a 1 Hz low-pass filter to all the synthetic data and add noise to the radial components. The noise is generated by first filtering the white noise in the same frequency band as the data, and then scaled according to a pre-defined signal to noise ratio (8.7 dB).

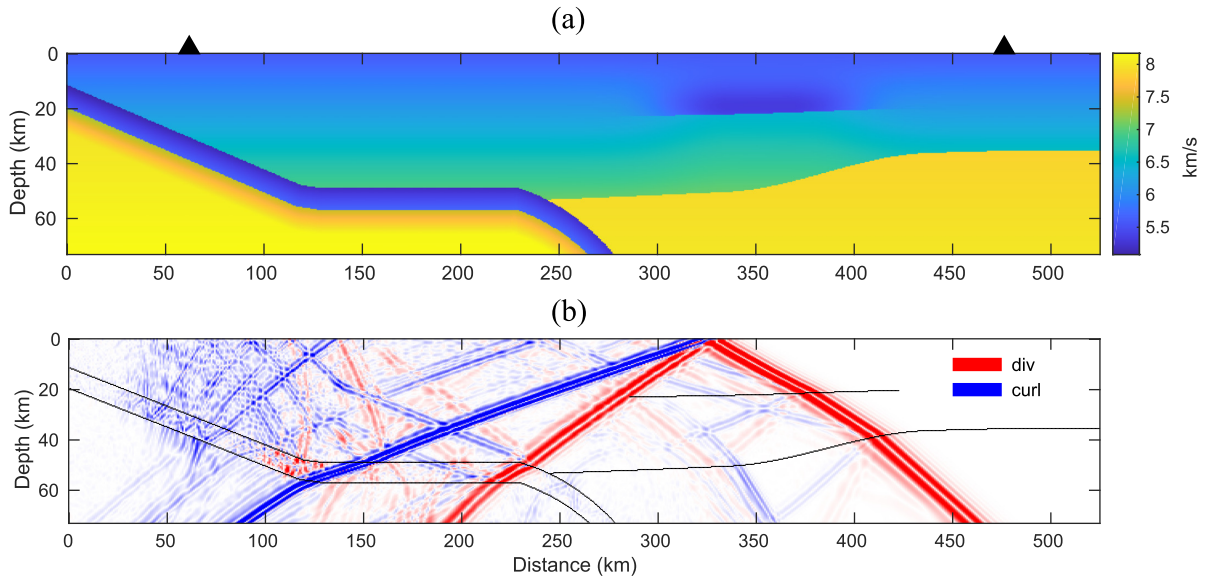

Figure 2. (a) The *P*-wave velocity model based on a flat subduction scenario to generate synthetic data. The two black triangles indicate the first and last station of the virtual dense seismic array. Main features to be captured by a RF profile include the low-velocity oceanic crust, the continental Moho with a smooth topography and a mid-crust discontinuity on the continental side. (b) A snapshot of the simulated wavefield, with the divergence and curl showing the *P* and *S* wavefields, respectively.

3.2 RF estimation

We first estimate RFs from the noise-free synthetics as a proxy to the 'true' RFs, by applying conventional iterative time-domain deconvolution at individual stations (Fig. 3a). The 'true' RFs show features as expected, including negative and positive phases related to the top and bottom edges of the oceanic crust. On the continental side, Ps phases track well the lateral variation of Moho topography and the mid-crust discontinuity. We then estimate RFs from the noisy synthetics using conventional practices. We use the iterative time domain deconvolution for individual RFs and stack the RFs from the seven events for the final RFs (Fig. 3b). Compared with the 'true' RFs (Fig. 3a), main phases in Fig. 3(b) are trackable. However, weaker phases (e.g. mid-crust discontinuity) are distorted and less coherent among nearby stations. In the meanwhile, a larger number of small incoherent phases downgrade the overall resolution of the image. Because the incoherent phases are not related to any real subsurface discontinuities, we attribute them to noise introduced by the deconvolution operations.

Finally, we estimate RFs from the same noisy data but using our new array-based deconvolution method. At each station, we joint invert the data from a subarray of five stations and all seven events for a RF with a minimum number of phases required by data. Fig. 4 shows an example of the iterative process at one subarray, with a four-phase RF providing a residual distribution statistically indistinguishable from a fully converged RF. In other words, this synthetic data set with noise can only resolve four phases in RF. Interestingly, the standard deviation of the residuals (σ_c) for our converged RF is close to that of the 'true' RFs (σ_t), while the one for conventional RFs (Fig. 3b) is substantially lower (σ_s), suggesting data overfitting by the large number of phases included in the time-domain iterative deconvolution method. Fig. 5 shows the three sets of RFs for the subarray and their waveform fittings. The array-based RFs are much simpler, yet are able to fit the data equally well as the reference and the conventional ones. Several weak phases in the 'true' RFs (e.g. the negative phase at ∼8 s) that are free-surface multiples are missing in our RFs. These missing phases do not improve data fitting in a statistically significant way and are considered unresolvable in our method. To resolve them we will need to either include more data or reduce the data uncertainty.

The full array-based RF image (Fig. 3c) agree well with the reference RF image (Fig. 3a), with major phases from the low-velocity oceanic crust and the continental Moho well resolved and tracked along the profile. Weaker phases, such as those corresponding to the mid-crust discontinuity, are now clearly resolved along the right distance range with the right amplitudes. At small distance range, the phases at ∼10 s is the only resolvable free-surface multiple. Other multiples, for example, the negative phase at 10 s between 50 and 200 km, are not included into the image according to our criterion of determining the number of phases. Moreover, incoherent noise is completely absent in the image and the whole profile is of better interpretability.

In this synthetic test, our input subsurface structures are laterally coherent, such that our assumptions on RF coherence are largely true. For point diffractors or sharp lateral discontinuities (e.g. Fig. 1a), the assumptions may not hold unless the diffracted wave is well sampled by a dense array. Otherwise, the array-based RF estimation may suppress the sharpness of the structure.

4 APPLICATION

Recent deployments of large-N arrays demonstrated the importance of capturing full seismic wavefields in future seismic imaging

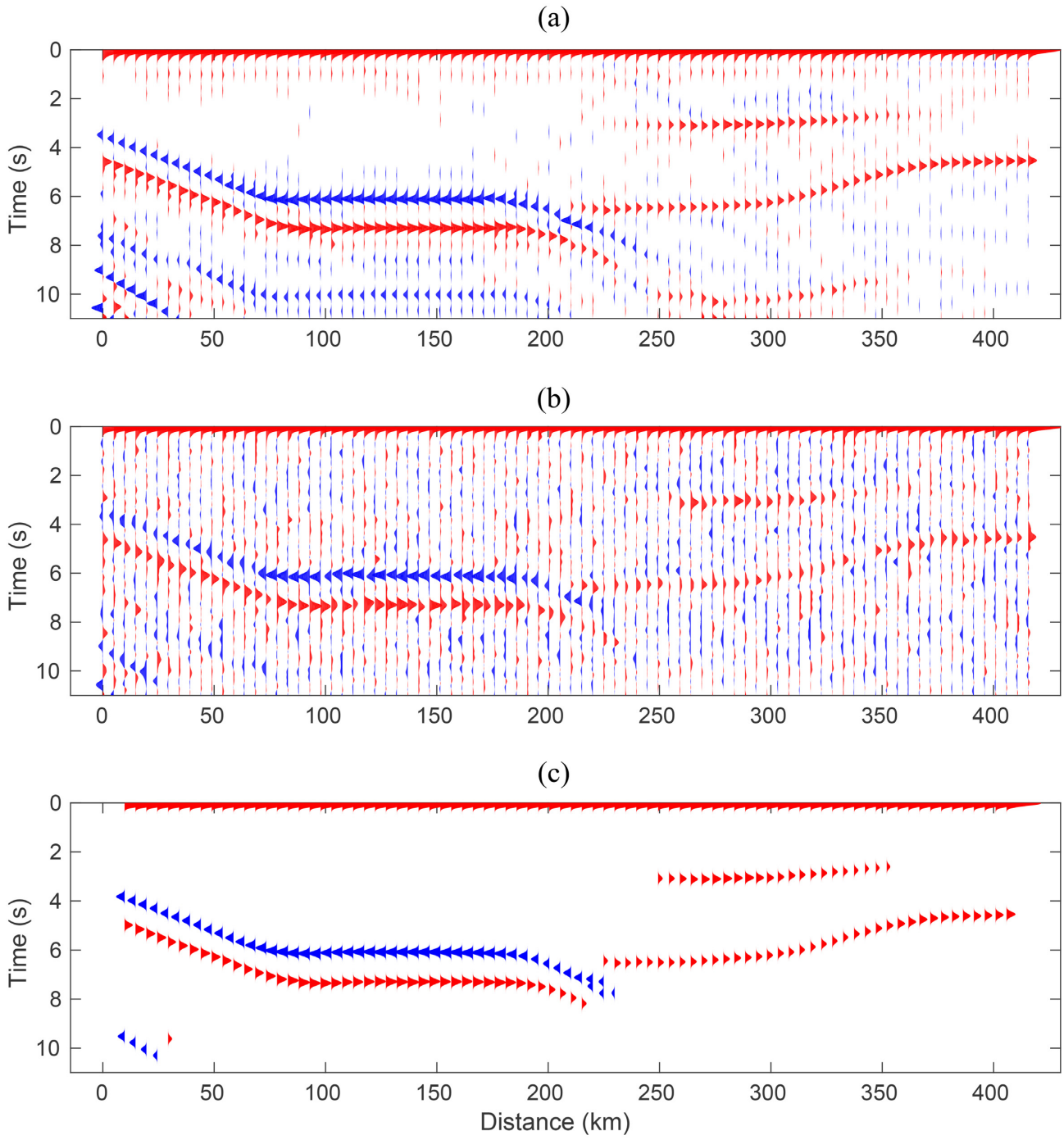

Figure 3. (a) Reference RFs estimated from the noise-free synthetics of the centre event at 40° using the iterative time-domain deconvolution method. (b) Conventional RFs obtained by stacking the RFs estimated separately from the noisy synthetic data of the seven events with noise. (c) RFs estimated with the new array-based method by jointly inverting the noisy synthetic data of all seven events.

projects (e.g. Lin *et al.* 2013; Ward & Lin 2017; Liu *et al.* 2018). Here we apply our array-based RF method to the data from the 2016 IRIS community wavefield experiment in northern Oklahoma (Sweet *et al.* 2018) to demonstrate the benefit of applying our method to dense arrays. Conventional RF estimation relies on stacking many RFs to suppress noise and artefacts. This is feasible because broad-band seismic experiments often last for a few months to a few years and record tens to hundreds of teleseismic events. However, nodal-type sensors typically operate for only a few weeks due to battery life, limiting the number of available events. How to retrieve high quality RFs from dense but short-duration deployments is a key challenge.

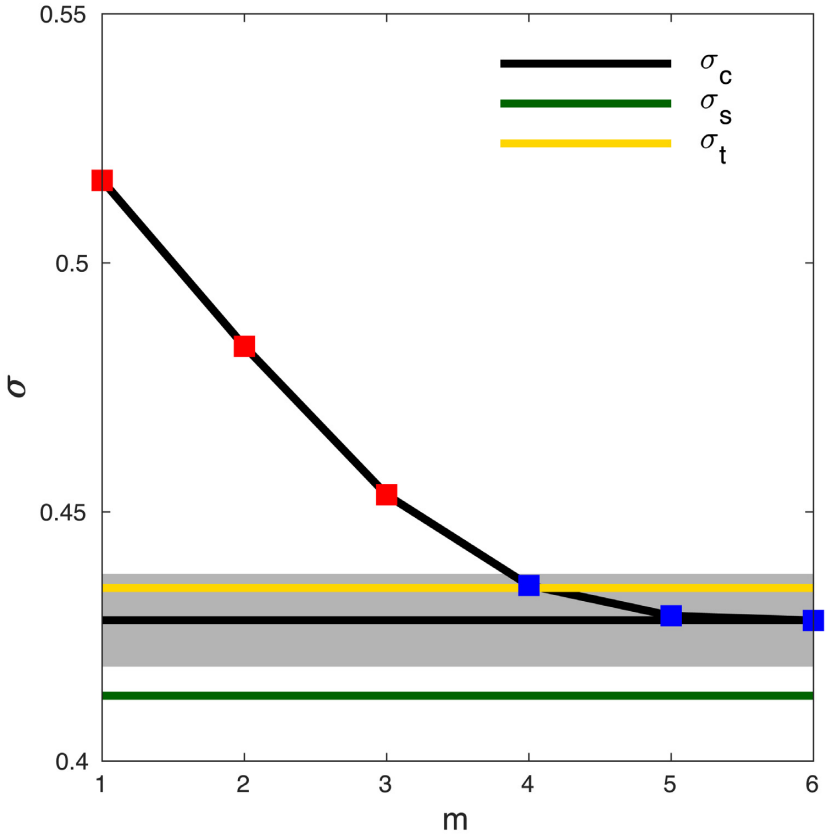

Figure 4. Standard deviation of residuals σ versus the number of phases m included in the RF inversions. Black line indicates the converged/stabilized value σ_c. The grey zone shows the bootstrapping 1 σ confidence interval around σ_c, given the number of data points used in the inversion. We pick the first blue square within the gray zone with $m = 4$ as our preferred RF. The yellow and green lines indicate the residual standard deviation for the 'true' RFs (σ_t) and the conventional stacked RFs (σ_s), respectively.

4.1 RF estimation

One major component of the IRIS experiment is three dense profiles of three-component nodal seismic sensors, with an even spacing of about 100 m (Fig. 6a). Given the small station spacing and array aperture, we focus on using RF to probe the shallow sedimentary structures. During the 1-month experiment, there were three $M_w \geq 5.5$ teleseismic events with good signal to noise ratios, two from Ecuador and one from Japan (Fig. 6b). We assume the station-side structural response of the three events are the same, because the piercing points of their incoming P waves for the shallow sedimentary structures are very close. This allows us to jointly invert the data from the three events. To resolve the shallow structures, we include more high frequency waveforms (0.2–2.5 Hz) in the inversion. In order to model the residuals with Gaussian distributions, we find it necessary to perform spectral whitening. We estimate the spectrum power of vertical component and divide it from both radial and vertical components.

We first estimate RFs using the conventional practices: we derive individual RFs through iterative time domain deconvolution for each event-station pair and then stack. The resulting RFs along the three profiles (Figs 7a–c) consistently show a weak first P phase and several closely following positive phases before 1 s, suggesting the existence of shallow slow structures. However, the phases are not coherent and hard to interpret. Later in the time window, we can see a few other phases that display better coherency across the array: a weak negative phase at 1 s, a strong positive phase at 1.5 s followed by some less coherent negative phases between 1.8 and 2.3 s. The coherency of these phases across the arrays and consistency of the three RF profiles suggests approximately flat layered shallow structures beneath the arrays. However, more detailed interpretation for structures is difficult, because of the limited resolution.

We then apply our array-based RF deconvolution method to the same data. Each RF estimation is done by joint inversion of the three events recorded by a five-station subarray. Fig. 8 shows an example of the iterative process for one subarray, where five coherent phases produce a residual distribution statistically indistinguishable from RF with more phases. The corresponding conventional RF produces slightly smaller residuals, but still statistically indistinguishable from that of the array-based RF. In Fig. 9, we show the two sets of RFs and their corresponding waveform fittings for the subarray. The conventional RFs are of lower resolution, especially in the first 1 s. Spurious phases are introduced due to overfitting. In contrast, the array-based RFs are simple and of high resolution. The uncertainty of phase timing is indicated by the green bar next to the phase representing 95 per cent confidence interval.

The full array-based RF profile in Figs 7(d)–(f) show high phase coherency and essentially flat structures. The first 1 s following

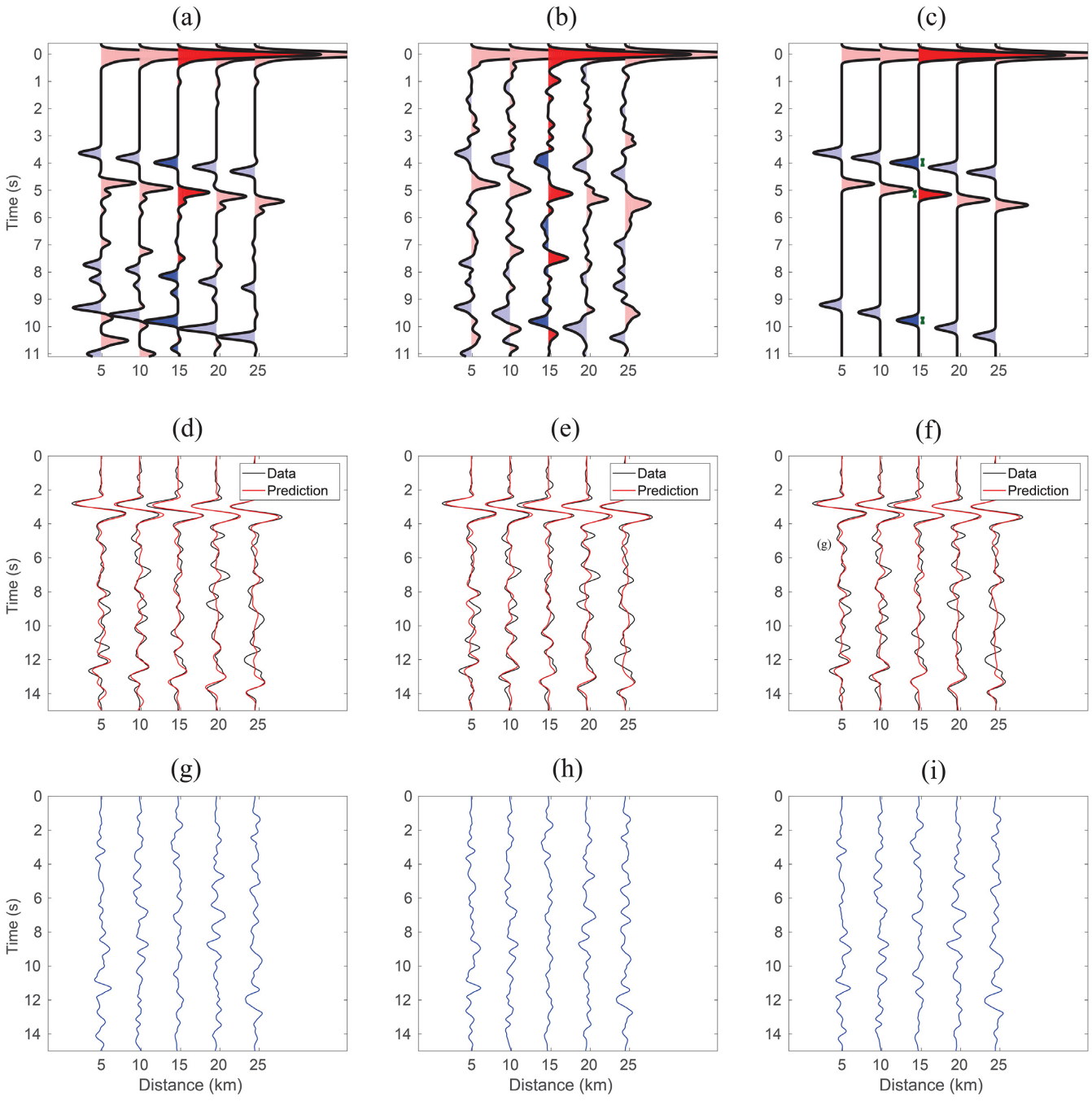

Figure 5. (a–c) display the true RFs, the conventional stacked RFs, and the array-based RFs for one five-station subarray, respectively. The phases at centre station are showed in darker colours. The green bars next to the phases in (c) indicate the 95 per cent confidence interval of the phase timing. (d–f) Waveform fitting for the true RFs, the stacked RFs and the array-based RFs, respectively for the centre event at 40°. The waveform in black is the radial component and waveform the red is the predicted radial component by convolving the vertical component with the estimated RF. (g–i) Waveform residuals (i.e. the difference between radial component and the prediction) for the true RFs, the stacked RFs, and the array-based RFs.

the direct *P* phases of the RFs, which the conventional method resolve poorly, now consists of two distinct positive phases trackable throughout the three profiles. We also obtain coherent positive and negative phase at about 1.5 and 2 s, respectively, consistent with the smeared features in the conventional RFs. Interestingly, the weak but seemingly coherent negative phases at ∼1 s in the conventional RF profiles are absent in the array-based RF profiles. We carefully examine this phase and conclude that it is a spurious phase caused by ringing effect, that is side-lobes, in the conventional method of deconvolution. The negative phase has opposite polarity and strong trade-offs with the two nearby positive phases. As a greedy algorithm without adjustment to existing phases, conventional iterative

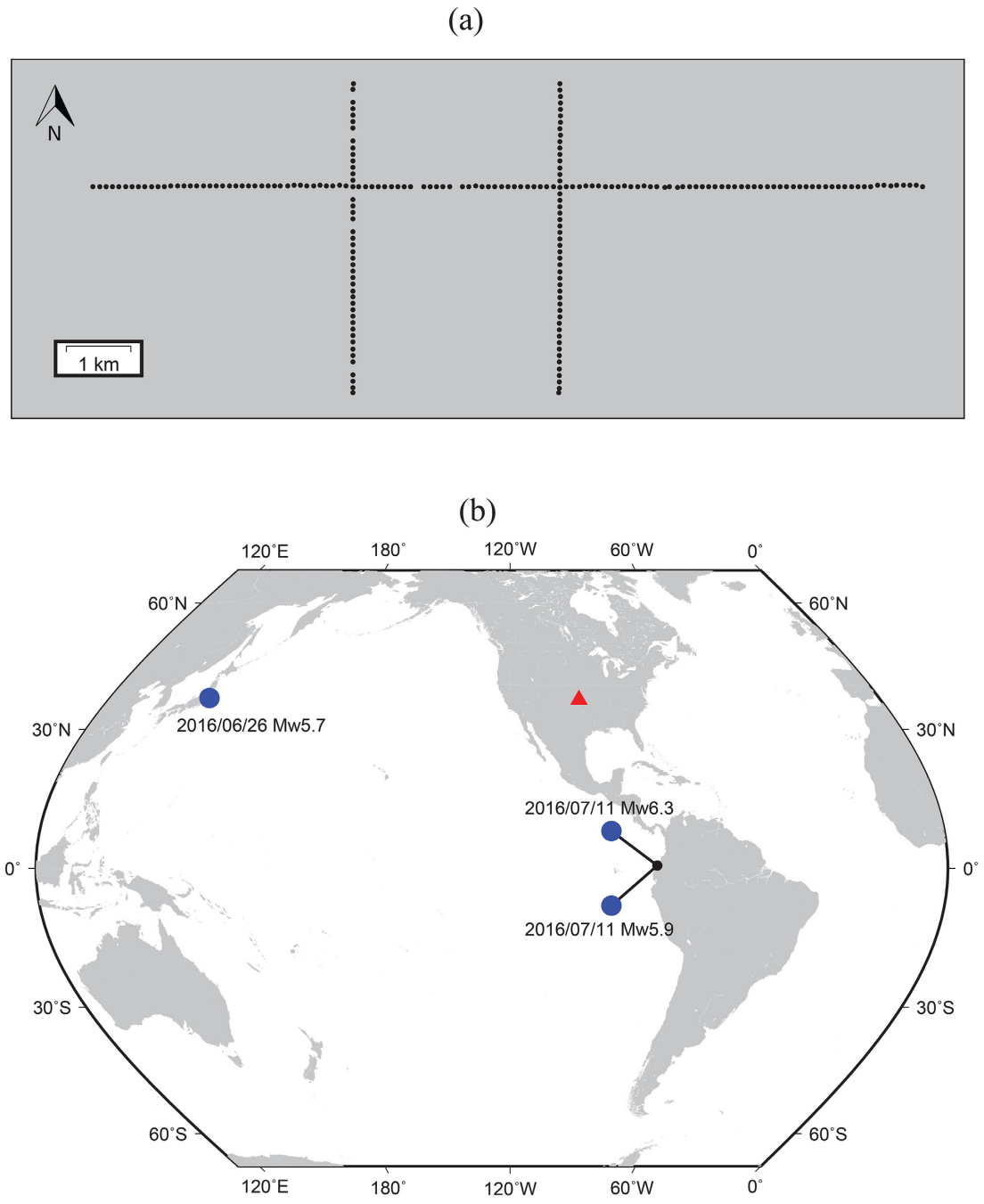

Figure 6. (a) Three nodal seismic lines deployed in the IRIS community wavefield experiment in Oklahoma. The station spacing is about 100 m. There are 129 and 49 nodes in the WE and NS profiles, respectively. (b) The three teleseismic events (blue dots) we use for the RF estimations: the 2016 July 11 earthquake doublet in Ecuador and the 2016 June 26 earthquake in Japan.

time-domain deconvolution cannot account for this trade-off and may produce this spurious phase before contributions from other phases are fully accounted for.

Our array-based RF profiles suggest relatively simple and uniform shallow structures beneath this region. We suggest that the two positive phases closely following first *P* phase are Ps phases linking to two shallow sedimentary discontinuities. The later positive phase at 1.5 s and the negative phase at 2 s can be the multiples, that is PpPs and PpSs/PsPs, or represent two shallow crustal discontinuities with increasing and decreasing velocity downwards, respectively. Further geological interpretation would benefit from other geophysical measurements (e.g. surface wave dispersions, boreholes) and the local geological history.

Besides showing the overall improved clarity of the RF profile, this real data application demonstrates that our new method

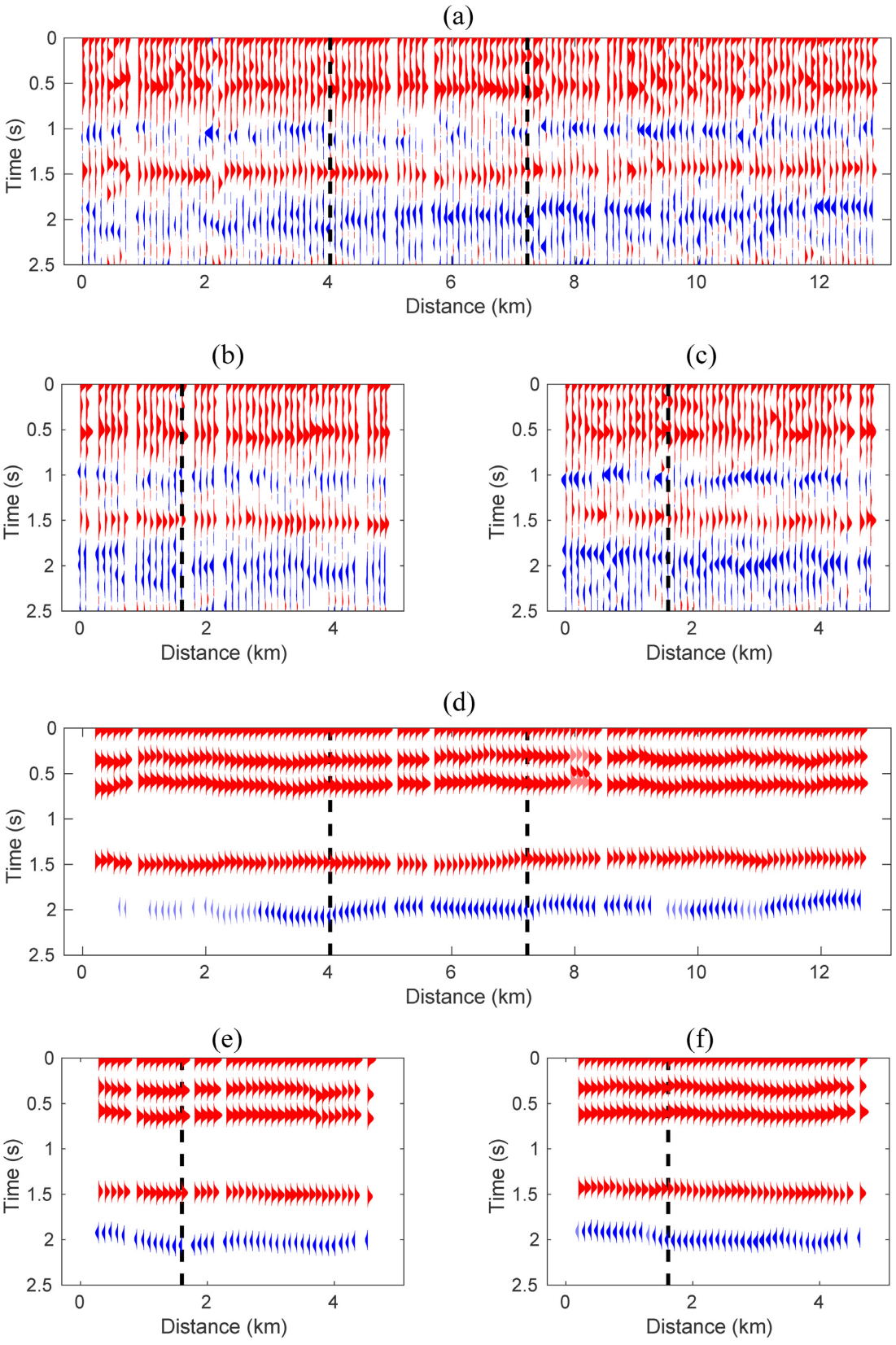

Figure 7. (a–c) Conventional stacked RFs along the W–E line, western N–S line and eastern N–S line of the IRIS wavefield experiment, respectively. The black dashed lines show the cross points of the profiles. (d–f) The same as (a–c) but for our array-based RFs. For parts of the RF profiles, light blue or light red colours indicate phases added after one more iteration beyond the stopping criteria. In other words, they are not as well resolved as the ones in blue or red colours.

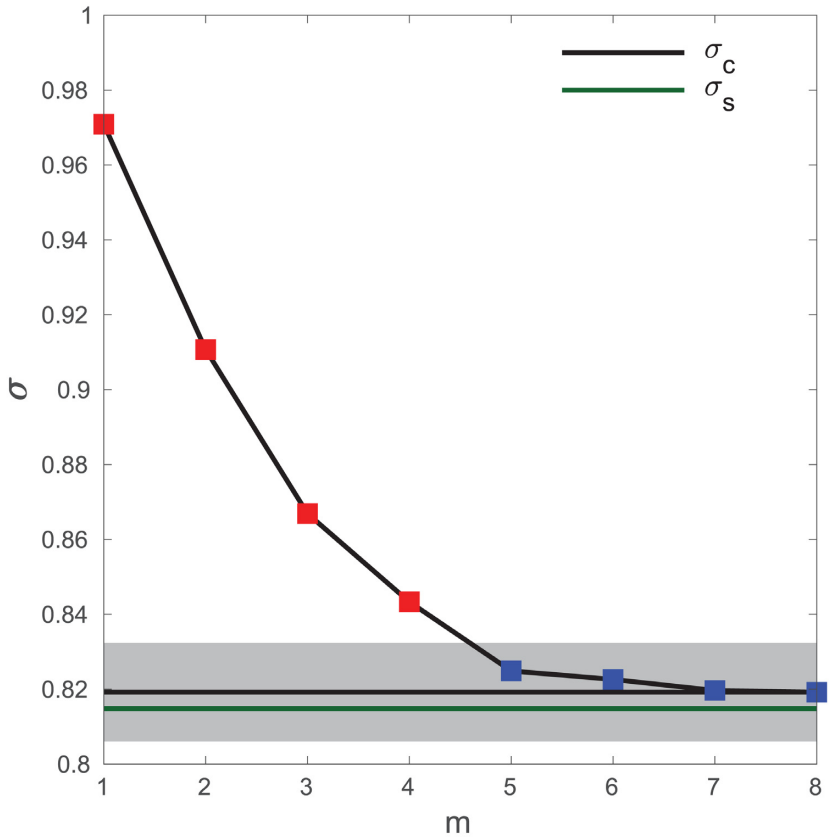

Figure 8. The same as Fig. 4 but for the real data application to one subarray in the IRIS wavefield experiment. We pick the first blue square within the grey zone with $m = 5$ as our preferred RF, with exceptions of $m = 4$ at several subarrays.

has advantages over conventional methods in resolving more features, especially interfering phases and removing noise introduced by the side-lobe effects of deconvolution. Indeed, compared with the conventional method, our proposed method is more complex and computationally more costly to deliver these advantages. In practice, sufficient stacking of conventional RFs (e.g. long-term or permanent stations) might produce RF images of high quality at lower cost. However, for short-term dense-array deployments (e.g. 1 month) where only a limited number of earthquakes are available, strong artifacts can exist in conventional RF profiles due to insufficient stacking. Our new method provides a solution to such scenarios.

5 CONCLUSIONS AND FUTURE WORK

Motivated by the emerging three-component large-N arrays, we develop a new array-based RF deconvolution method towards coherent RF profiles with only phases required by data. To address common issues such as non-uniqueness and data overfitting in conventional deconvolution methods, we cast RF estimation as a sparsity-prompting inverse problem and exploit the wavefield coherency on dense arrays. Synthetic test shows that this new method outperforms conventional practices and produces RF profiles with higher fidelity and resolution. The real-data application to dense nodal seismic profiles also demonstrates the new method's advantages over conventional practices in producing higher-quality RF images with small amounts of data available on short-term dense deployments. Compared with the conventional method, our method comes with higher computational cost due to non-linear inversion and the sampling of parameter space.

Uncertainty estimation of phase timings is valuable new information provided by this method. Theoretically, estimating RFs as an inverse problem allows us to rigorously quantify RF uncertainties, which can be valuable during geological interpretations. As discussed in Sections 2.3 and 2.4, we analyse the NA ensembles and the residual statistics to estimate the uncertainties. However, our experiments show that NA's efficiency drops quickly as the number of phases increases (e.g. beyond 10). Furthermore, NA does not perform importance sampling of the model posterior probability distribution, and the accuracy of the ensemble appraisal approach we use relies on thorough exploration of the model space (Sambridge 1999b). Therefore, our current RF uncertainty estimation approach may be biased, especially when a large number of phases are required by data. In the future, we may use more efficient algorithms, for example, parallel Metropolis–Hastings algorithm (Jacob *et al.* 2010), to sample the model space and improve the uncertainty estimates.

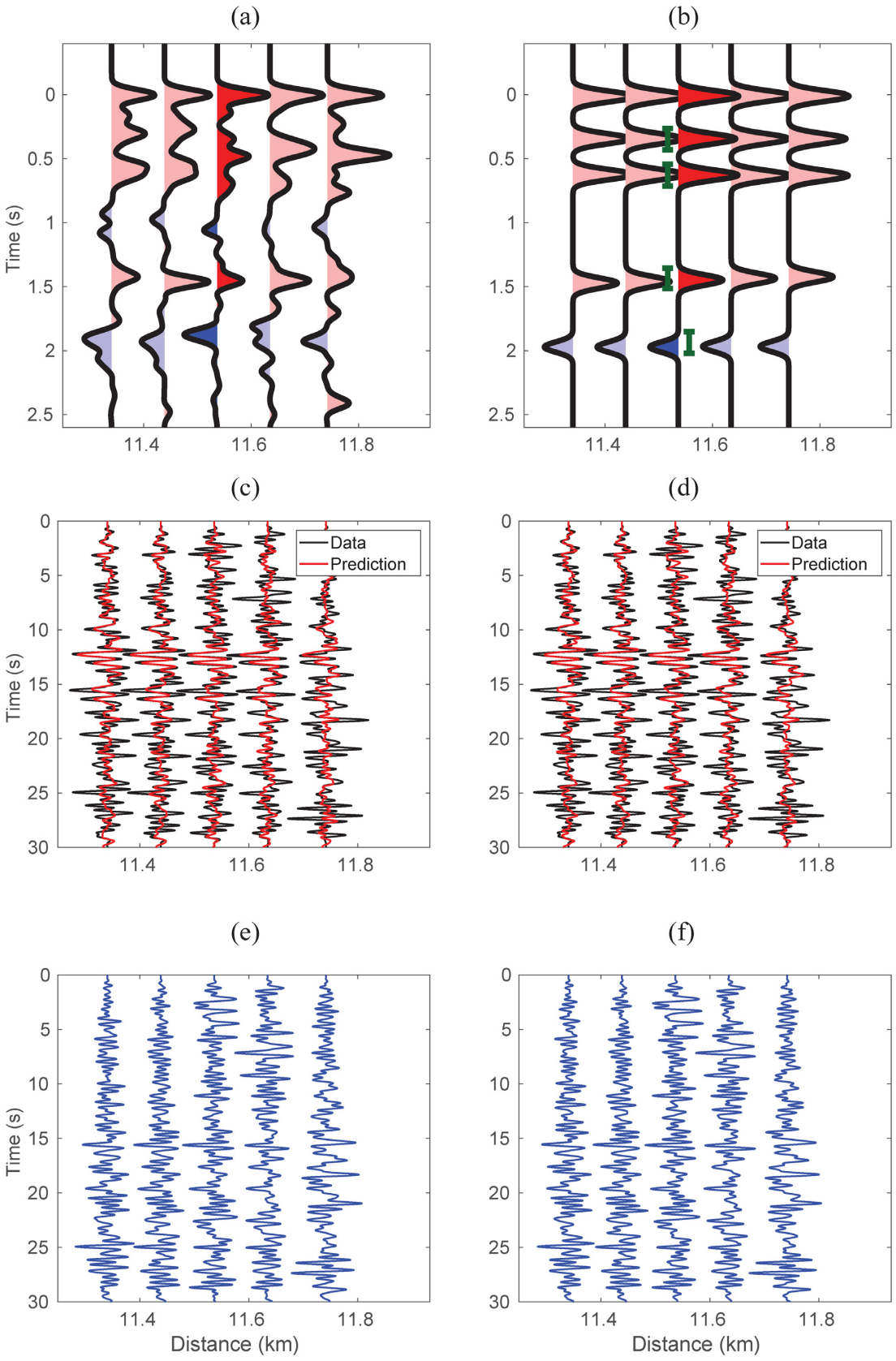

Figure 9. Similar to Fig. 5 but for the real data application to one subarray in the IRIS wavefield experiment. (a, c, e) are for the conventional stacked RFs and (b, d, f) are for our array-based RFs. (c, e, d, f) are based on the waveforms of M_w 6.3 event.

ACKNOWLEDGEMENTS

We thank the team of IRIS community wavefield experiment for deployments and making the data readily accessible through IRIS Data services (Anderson *et al.* 2016). We thank Rob Clayton and YoungHee Kim for helpful conversations. We thank Elmer Ruigrok and an anonymous reviewer for providing constructive reviews. This research is financially supported by NSF grant 1722879.

REFERENCES

Ammon, C.J., 1991. The isolation of receiver effects from teleseismic P waveforms. *Bull. seism. Soc. Am.,* **81,** 2504–2510.

Ammon, C.J., Randall, G.E. & Zandt, G., 1990. On the nonuniqueness of receiver function inversions. *J. geophys. Res.,* **95,** 15303, doi:10.1029/JB095iB10p15303.

Anderson, K., Sweet, J. & Woodward, B., 2016. IRIS Community Wavefield Experiment in Oklahoma, Incorporated Research Institu- tions for Seismology. Other/Seismic Network, doi: 10.7914/SN/ YW_2016.

Aster, R.C., Borchers, B. & Thurber, C.H., 2019. *Parameter Estimation and Inverse Problems,* Elsevier.

Bostock, M.G. & Rondenay, S., 1999. Migration of scattered teleseismic body waves. *Geophys. J. Int.,* **137,** 732–746.

Chen, L., Wen, L. & Zheng, T., 2005a. A wave equation migration method for receiver function imaging: 1. Theory. *J. geophys. Res.,* **110,** B11309, doi:10.1029/2005JB003665.

Chen, L., Wen, L. & Zheng, T., 2005b. A wave equation migration method for receiver function imaging: 2. Application to the Japan subduction zone. *J. geophys. Res.,* **110,** B11310, doi:10.1029/2005JB003666.

Clayton, R.W. & Wiggins, R.A., 1976. Source shape estimation and deconvolution of teleseismic bodywaves. *Geophys. J. Int.,* **47,** 151–177.

Crotwell, H.P. & Owens, T.J., 2005. Automated receiver function processing. *Seismol. Res. Lett.,* **76,** 702–709.

Dueker, K.G. & Sheehan, A.F., 1997. Mantle discontinuity structure from midpoint stacks of converted P to S waves across the Yellowstone hotspot track. *J. geophys. Res.,* **102,** 8313–8327.

Duputel, Z., Rivera, L., Fukahata, Y. & Kanamori, H., 2012. Uncertainty estimations for seismic source inversions. *Geophys. J. Int.,* **190,** 1243–1256.

Eagar, K.C., Fouch, M.J., James, D.E. & Carlson, R.W., 2011. Crustal structure beneath the High Lava Plains of eastern Oregon and surrounding regions from receiver function analysis. *J. geophys. Res.,* **116,** B02313, doi:10.1029/2010JB007795.

Fischer, K.M., Ford, H.A., Abt, D.L. & Rychert, C.A., 2010. The lithosphere-asthenosphere boundary. *Annu. Rev. Earth Planet. Sci.,* **38,** 551–575.

Gilbert, H.J., Sheehan, A.F., Dueker, K.G. & Molnar, P., 2003. Receiver functions in the western United States, with implications for upper mantle structure and dynamics. *J. geophys. Res.,* **108,** doi:10.1029/2001JB001194.

Gurrola, H., Baker, G.E. & Minster, J.B., 1995. Simultaneous time-domain deconvolution with application to the computation of receiver functions. *Geophys. J. Int.,* **120,** 537–543.

Hansen, P.C., 1992. Analysis of discrete Ill-Posed problems by means of the L-Curve. *SIAM Rev.,* **34,** 561–580.

Jacob, P., Robert, C.P. & Smith, M.H., 2010. Using parallel computation to improve Independent Metropolis–Hastings based estimation, *J. Comput. Graph. Stat.,* **20**(3), 616–635.

Kim, Y, Miller, M.S., Pearce, F. & Clayton, R.W., 2012. Seismic imaging of the Cocos plate subduction zone system in central Mexico. *Geochem., Geophys. Geosys.,* **13**(7), doi:10.1029/2012GC004033.

Kim, Y., Clayton, R.W. & Jackson, J.M., 2010. Geometry and seismic properties of the subducting Cocos plate in central Mexico. *J. geophys. Res.,* **115,** B06310, doi:10.1029/2009JB006942.

Kolb, J.M. & Lekić, V., 2014. Receiver function deconvolution using transdimensional hierarchical Bayesian inference. *Geophys. J. Int.,* **197,** 1719–1735.

Kumar, P., Kind, R., Yuan, X. & Mechie, J., 2012. USArray receiver function images of the lithosphere-asthenosphere boundary. *Seismol. Res. Lett.,* **83,** 486–491.

Langston, C.A., 1979. Structure under Mount Rainier, Washington, inferred from teleseismic body waves. *J. geophys. Res.,* **84,** 4749, doi:10.1029/JB084iB09p04749.

Levander, A. & Miller, M.S., 2012. Evolutionary aspects of lithosphere discontinuity structure in the western U.S. *Geochem., Geophys. Geosys.,* **13**(7), doi:10.1029/2012GC004056.

Levander, A., Schmandt, B., Miller, M.S., Liu, K., Karlstrom, K.E., Crow, R.S., Lee, C.-T.A. & Humphreys, E.D., 2011. Continuing Colorado plateau uplift by delamination-style convective lithospheric downwelling. *Nature,* **472,** 461–465.

Li, D., Helmberger, D., Clayton, R.W. & Sun, D., 2014. Global synthetic seismograms using a 2-D finite-difference method. *Geophys. J. Int.,* **197,** 1166–1183.

Ligorría, J.P. & Ammon, C.J., 1999. Iterative deconvolution and receiver-function estimation. *Bull. seism. Soc. Am.,* **89**(5), 1395–1400.

Lin, F.-C., Li, D., Clayton, R.W. & Hollis, D., 2013. High-resolution 3D shallow crustal structure in Long Beach, California: application of ambient noise tomography on a dense seismic array. *Geophysics,* **78,** Q45–Q56.

Liu, G., Persaud, P. & Clayton, R.W., 2018. Structure of the Northern los angeles basins revealed in teleseismic receiver functions from short-term nodal seismic arrays. *Seismol. Res. Lett.,* **89,** 1680–1689.

Ma, Y. & Clayton, R.W., 2016. Structure of the Los Angeles Basin from ambient noise and receiver functions. *Geophys. J. Int.,* **206,** 1645–1651.

Miller, M.S. & Piana Agostinetti, N., 2012. Insights into the evolution of the Italian lithospheric structure from S receiver function analysis. *Earth planet. Sci. Lett.,* **345–348,** 49–59.

Nikulin, A., Levin, V. & Park, J., 2009. Receiver function study of the Cascadia megathrust: evidence for localized serpentinization. *Geochem., Geophys. Geosys.,* **10**(7), doi:10.1029/2009GC002376.

Nábelek, J. *et al.*, 2009. Underplating in the Himalaya-Tibet collision zone revealed by the Hi-CLIMB experiment. *Science,* **325,** 1371–1374.

Park, J. & Levin, V., 2000. Receiver functions from multiple-taper spectral correlation estimates. *Bull. seism. Soc. Am.,* **90,** 1507–1520.

Sambridge, M., 1999a. Geophysical inversion with a neighbourhood algorithm–I. Searching a parameter space. *Geophys. J. Int.,* **138,** 479–494.

Sambridge, M., 1999b. Geophysical inversion with a neighbourhood algorithm–II. Appraising the ensemble. *Geophys. J. Int.,* **138,** 727–746.

Schulte-Pelkum, V. & Mahan, K.H., 2014. A method for mapping crustal deformation and anisotropy with receiver functions and first results from USArray. *Earth planet. Sci. Lett.,* **402,** 221–233.

Shen, W., Ritzwoller, M.H. & Schulte-Pelkum, V., 2013. A 3-D model of the crust and uppermost mantle beneath the Central and Western US by joint inversion of receiver functions and surface wave dispersion. *J. geophys. Res.,* **118,** 262–276.

Sweet, J.R. *et al.*, 2018. A community experiment to record the full seismic wavefield in Oklahoma. *Seismol. Res. Lett.,* **89,** 1923–1930.

Tarantola, A. 2005 *Inverse Problem Theory and Methods for Model Parameter Estimation,* Vol. **89,** SIAM.

Tauzin, B., van der Hilst, R.D., Wittlinger, G. & Ricard, Y., 2013. Multiple transition zone seismic discontinuities and low velocity layers below western United States. *J. geophys. Res.,* **118,** 2307–2322.

Vinnik, L.P., 1977. Detection of waves converted from P to SV in the mantle. *Phys. Earth planet. Inter.,* **15,** 39–45.

Wang, Y. & Pavlis, G.L., 2016. Generalized iterative deconvolution for receiver function estimation. *Geophys. J. Int.,* **204,** 1086–1099.

Wapenaar, K., van der Neut, J., Ruigrok, E., Draganov, D., Hunziker, J., Slob, E., Thorbecke, J. & Snieder, R., 2011 Seismic interferometry by crosscorrelation and by multidimensional deconvolution: a systematic comparison. *Geophys. J. Int.,* **185,** 1335–1364.

Ward, K.M. & Lin, F., 2017. On the viability of using autonomous three-component nodal geophones to calculate teleseismic *Ps* receiver functions with an application to old faithful, Yellowstone. *Seismol. Res. Lett.,* **88,** 1268–1278.

Ward, K.M., Lin, F. & Schmandt, B., 2018. High-resolution receiver function imaging across the Cascadia subduction zone using a dense nodal array. *Geophys. Res. Lett.,* **45,** 12 218–12 225.

Wilson, D. & Aster, R., 2005. Seismic imaging of the crust and upper mantle using regularized joint receiver functions, frequency–wave number filtering, and multimode Kirchhoff migration. *J. geophys. Res.,* **110,** B05305, doi:10.1029/2004JB003430.

Xu, Z.J., Song, X. & Zhu, L., 2013. Crustal and uppermost mantle S velocity structure under Hi-CLIMB seismic array in central Tibetan Plateau from joint inversion of surface wave dispersion and receiver function data. *Tectonophysics,* **584,** 209–220.

Yagi, Y. & Fukahata, Y., 2008. Importance of covariance components in inversion analyses of densely sampled observed data: an application to waveform data inversion for seismic source processes. *Geophys. J. Int.,* **175,** 215–221.

Yang, X., Pavlis, G.L. & Wang, Y., 2016. A quality control method for teleseismic *P* -wave receiver functions. *Bull. seism. Soc. Am.,* **106,** 1948–1962.

Yildirim, S., Cemgil, A.T., Aktar, M., Ozakin, Y. & Ertuzun, A., 2010. A Bayesian deconvolution approach for receiver function analysis. *IEEE Trans. Geosci. Remote Sens.,* **48,** 4151–4163.

Zhu, L. & Kanamori, H., 2000. Moho depth variation in southern California from teleseismic receiver functions. *J. geophys. Res.,* **105,** 2969–2980.